

Barycenter Self-Adapting Triboelectric Nanogenerator for Sea Water Wave High-Entropy Energy Harvesting and Self-Powered Forecasting in Marine Meteorology

Yuhan Yang, Jing Wen, Furong Chen,* Yutao Hao, Xiaobo Gao, Tao Jiang, Baodong Chen,* and Zhong Lin Wang*

As a high entropy energy (HEE), irregular seawater waves are a promising source of sustainable energy, and the development of matched harvesting technology is imperative to accommodate the new era. Here, a barycenter self-adapting triboelectric nanogenerator (BSA-TENG) that addresses these concerns and shows its applications as a distributed power source in isolated waters is reported. Benefitting from the physical gravity-guided structure design, random vibrational water wave HEE can be effectively converted into rotational mechanical energy and then converted into electric energy. In a nonlinear seawater wave pool, a unit delivers a peak power of 0.1 mW under a load resistance of 500 M Ω when the working frequency is <1 Hz. On this basis, a self-powered temperature sensor system and wireless signal transmitter have been developed and driven entirely by the BSA-TENG. This work plays a key role in promoting ocean HEE harvesting and provides a workable way for a self-powered service system in seawater wave and marine meteorology monitoring and forecasting.

1. Introduction

With the booming of the Internet of Things (IoTs)^[1] and 5G information age, the marine meteorology field has also been greatly influenced by technical advances, entering the digital age. Digital forecasting services, including seawater wave, ocean temperature, relative humidity, sea-level air pressure, and sea-level altitude data statistics and analysis, can effectively help forecasters make decisions and are becoming an indispensable means for monitoring and warning and make forecasting more accurate. Real-time data acquisition relies on billions of electronic devices and sensor networks, which are generally powered by traditional energy technologies, such as solar energy, wind power, and batteries. Considering the limited lifetime, frequent replacement, high recharging costs of existing technology

in a corrosive marine environment, and unsuspected environmental factors, exploit new power technology is necessary.

At present, there are basically two types of common power sources: traditional concentrated and distributed supply.^[2] A distributed power supply is used to utilize whatever is available in the environment in which the device is deployed to obtain energy.^[3] For the current IoTs, electrical equipment is widely distributed and possibly moving, and they must be powered by distributed power. The energy distribution for the era of IoTs can also be understood from entropy theory.^[4] In thermodynamics for describing molecular motion and temperature, entropy is used to describe the disorder or randomness of a system. This means that the distributed power in the era of IoTs would follow the theory of high entropy energy (HEE).^[2] Distributed HEE sources can be solar cells, wind energy, body motion energy, vibration energy, thermal energy, and chemical energy.^[5] Under the background of carbon neutrality, facing the distributed power need for these billions of electron devices and sensor networks, researchers are forced to develop a sustainable and maintenance-free HEE supply technology.

Ocean wave energy is one of the most desirable distributed energies for large-scope applications, with superior advantages of wide coverage abundant reserve, ever-present, and little

Y. Yang, J. Wen, T. Jiang, B. Chen, Z. L. Wang
Beijing Institute of Nanoenergy and Nanosystems
Chinese Academy of Sciences
Beijing 101400, P. R. China
E-mail: chenbaodong@binn.cas.cn; zlwang@binn.cas.cn

Y. Yang, F. Chen, Y. Hao, X. Gao
School of Materials Science and Engineering
Inner Mongolia University of Technology
Hohhot 010051, P. R. China
E-mail: cfr7075@imut.edu.cn

Y. Yang, Y. Hao, X. Gao, B. Chen
Institute of Applied Nanotechnology
Jiaxing, Zhejiang 314031, P. R. China

J. Wen, T. Jiang, B. Chen, Z. L. Wang
College of Materials Science and Opto-Electronic Technology
School of Nanoscience and Technology
University of Chinese Academy of Sciences
Beijing 100049, P. R. China

Z. L. Wang
School of Materials Science and Engineering
Georgia Institute of Technology
Atlanta, GA 30332, USA

 The ORCID identification number(s) for the author(s) of this article can be found under <https://doi.org/10.1002/adfm.202200521>.

DOI: 10.1002/adfm.202200521

dependence on the environmental conditions.^[6,7] The oceans contain abundant HEEs due to the ocean waves' constantly unordered fluctuations. Currently, most commercial energy harvesters in the sea still consist of electromagnetic generators (EMGs).^[8,9] Nevertheless, the main technology of these generators is a permanent magnet, which makes the device heavy, bulky, and costly, hindering most production of ocean wave energy harvesters.^[10] Thus, a matching technology that is portable, small, and low in cost is needed to efficiently harvest ocean HEE. The triboelectric nanogenerator (TENG, also called the Wang generator) was invented in 2012 as a promising technology for converting mechanical energy into electrical energy.^[11–15] Compared with EMGs, TENGs do not rely on bulky magnetic components. They adopt a working mechanism of Maxwell's displacement current,^[8,13,16,17] so they are more efficient and lighter, with a higher power density and lower manufacturing costs.^[8,11,13,16,18] To date, TENGs have exhibited huge potential in harvesting HEEs from a variety of mechanical energy sources, especially low-frequency ocean waves.^[19] Various TENG devices have been designed to efficiently harvest distributed ocean HEEs.^[14,15,20] However, most of the demonstrated TENG devices directly use the vibration of ocean waves to harvest the energy, and they have an oscillatory frequency close to the ocean wave triggering frequency.^[6,11,15,19,21] The extremely low frequency of ocean waves induces the TENG to generate low-frequency outputs, resulting in low average output performance.

Here, we propose a barycenter self-adapting triboelectric nanogenerator (BSA-TENG) fabricated by using 3D printing and a freestanding triboelectric layer, which can harvest low-frequency ocean HEEs through simple and effective physical gravity-guided structure design. The BSA-TENG can more easily self-adapt to random harvest and irregular HEE depending on the continuous movement of the device barycenter position and synchronous rotation of the central slip ring. The lightweight and durable BSA-TENG delivers a transferred charge of 22 nC and a peak power of 0.1 mW under an external load resistance of 500 M Ω when the working frequency is less than 1 Hz. Owing to its excellent performance, a self-powered temperature sensor and wireless signal transmitter system is demonstrated and driven entirely by the BSA-TENG, which can perform temperature sensing, sea water wave warning, and analytics to assist forecasters in decision making. This work plays a key role in promoting ocean HEE harvesting, opens new avenues for self-powered forecasting services in marine meteorology and sea data statistics, and may profoundly influence global climate observations.

2. Results and Discussion

Figure 1a depicts the BSA-TENG network working on the ocean surface around the island. The structural components of the BSA-TENG are shown in **Figure 1b** and mainly consist of four parts: 1) 3D printed resin housing; 2) dielectric balls; 3) dielectric film; and 4) Al electrodes. Among them, the 3D printed resin housing is assembled with bearings, shafts, slip rings, and central siphon as an external barycenter self-adapting structure. **Figure S1a** (Supporting Information) demonstrates that the

main composition includes three groups of unidirectional commutable baffles, three water inlets, and a rotating shaft in the middle. The dielectric balls, dielectric film, and Al electrodes constitute the major components of the BSA-TENG, which are shown in **Figure S1b** (Supporting Information). Photos of each component of the BSA-TENG are shown in **Figure S1c** (Supporting Information).

The BSA-TENG working state in ocean waves is shown in **Figure 1c**. When the BSA-TENG was working, water fluctuates downward into part 1 in downward waves from the water inlets, and the unidirectional commutable baffle between part 1 and part 3 bursts through so that water flows out from the open baffle. Then, the water fluctuates upward and flows into part 3 from the water inlets, while the water flows out of part 1. The status of the BSA-TENG when ocean waves fluctuate up and down is depicted in **Figure 2a**. During this process, water fills the right half of the BSA-TENG, and the barycenter changes from G_0 to G_1 , as depicted in **Figure 2b**. At this point, the BSA-TENG is deflected clockwise under gravity due to the self-adapting structure. The barycenter of the BSA-TENG shifts from G_1 to G_2 with the deflection. Next, the ocean wave fluctuates downward again; the unidirectional commutable baffle between part 1 and part 3 closes, and the water continues to flow into part 3. The barycenter of the structure shifts from G_2 to G_1 again, and the BSA-TENG continues to deflect clockwise until the unidirectional commutable baffle between part 2 and part 3 bursts through. With this as a period, the BSA-TENG has continuous unidirectional rotation under the water fluctuation.

With the continuous unidirectional rotation of the BSA-TENG, the internal components start to work. Its working principle is illustrated in **Figure S2c** (Supporting Information). By conjunction of the triboelectrification effect and electrostatic induction effect, physical contact between the dielectric film and the dielectric balls causes triboelectric charges on the two surfaces (**Figure S2c(I)**, Supporting Information); relative sliding between the dielectric film and the dielectric balls caused by external structural rotation results in an electric potential drop across the two electrodes built below the dielectric film, which drives the electrons to flow between the two to balance the electrostatic system (**Figure 2b(II)**)^[22] In the same principle, a potential difference between the two electrodes is created, and the electrons move in reverse as the external structure of the generator continues to rotate (**Figure 2b(III,IV)**). Cyclically, the BSA-TENG generates an alternating current. To better understand the output performance of the BSA-TENG, the potential distribution on the two electrodes at different states was simulated by using the finite element analysis method (commercial software of COMSOL Multiphysics). As shown in **Figure 2f(I)**, when the dielectric balls were in the middle of the two electrodes, the potential was zero. When the dielectric balls slide to the right electrode, the potential contour clearly shows the potential difference between the two electrodes in **Figure 2f(II)**, which would drive the current flowing in the external circuit. Then, as shown in **Figure 2f(III)**, the dielectric balls were at the middle of the two electrodes again, and the potential returned to zero. The potential contour clearly shows the opposite potential difference between the two electrodes in **Figure 2f(IV)**.

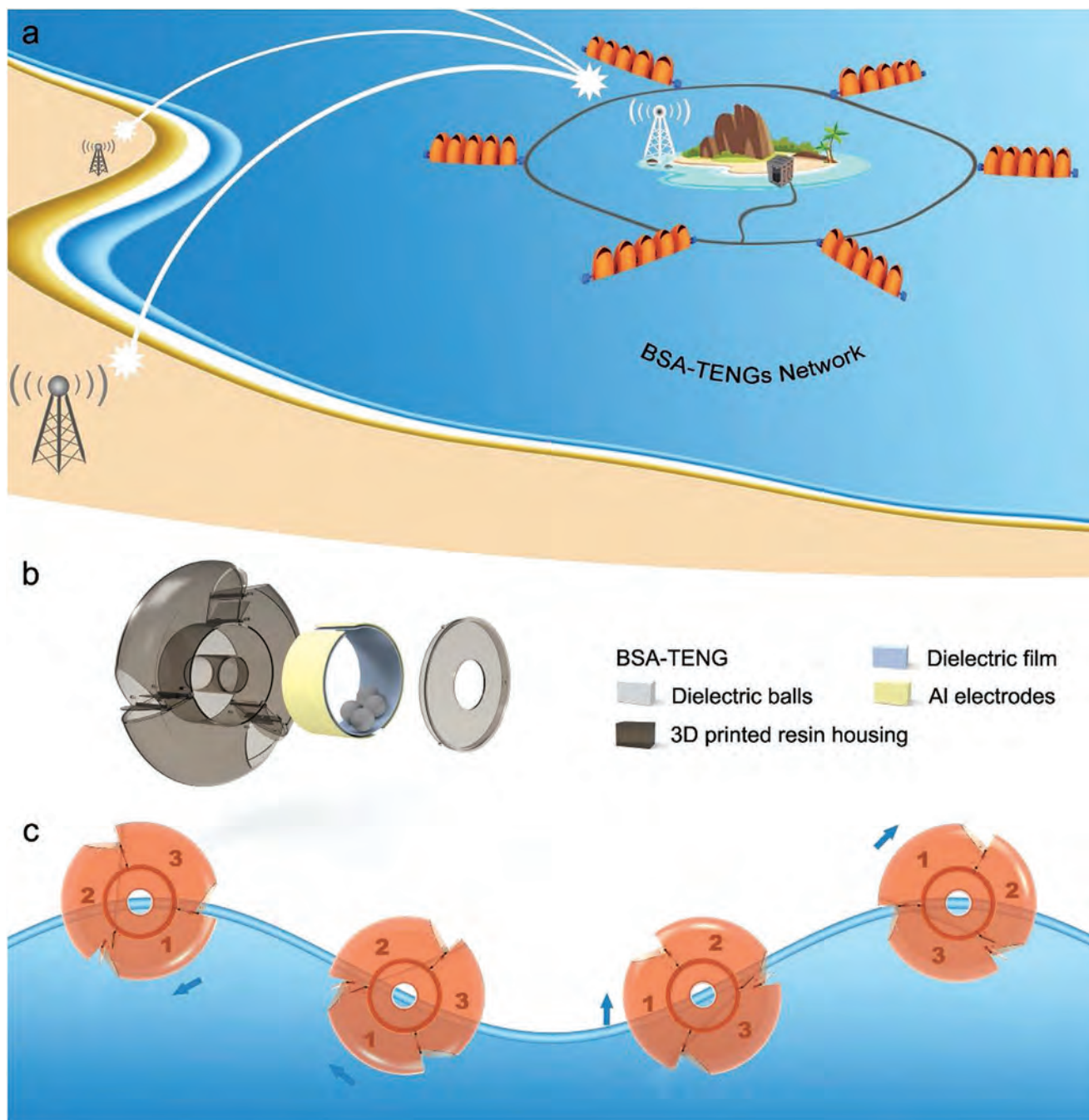


Figure 1. Application scenario and structural design of the BSA-TENG. a) Schematic diagram of the BSA-TENG network for harvesting ocean HEES around the island. b) Structural components of the BSA-TENG. c) Working state of the BSA-TENG in ocean waves.

The simulation results could obtain up to 3000 V. When the BSA-TENG had a 100 mm inside diameter and worked under a continuous mechanical trigger of 50 rpm, the open-circuit voltage waveform, transferred charge waveform, and short-circuit current waveform are displayed in Figure 2c–e. For the tribocharge saturated state, ≈ 26 nC of transferred charges, while the open-circuit voltage is estimated to be ≈ 69 V, and the short circuit current is ≈ 0.1 μ A. In the following sections, we will optimize and discuss the performance of the

BSA-TENG device, and finally, we demonstrate the feasibility of the system in the water harvesting high entropy energy around the island.

To comprehensively understand the performance of the BSA-TENG under an external mechanical trigger, the BSA-TENG was fixed on a motor that could rotate. The testing process with a mechanical trigger is shown in Figure S2b and Video S1 (Supporting Information). For ease of measurement, the motor rotating speed was fixed at 50 rpm. In this work, the

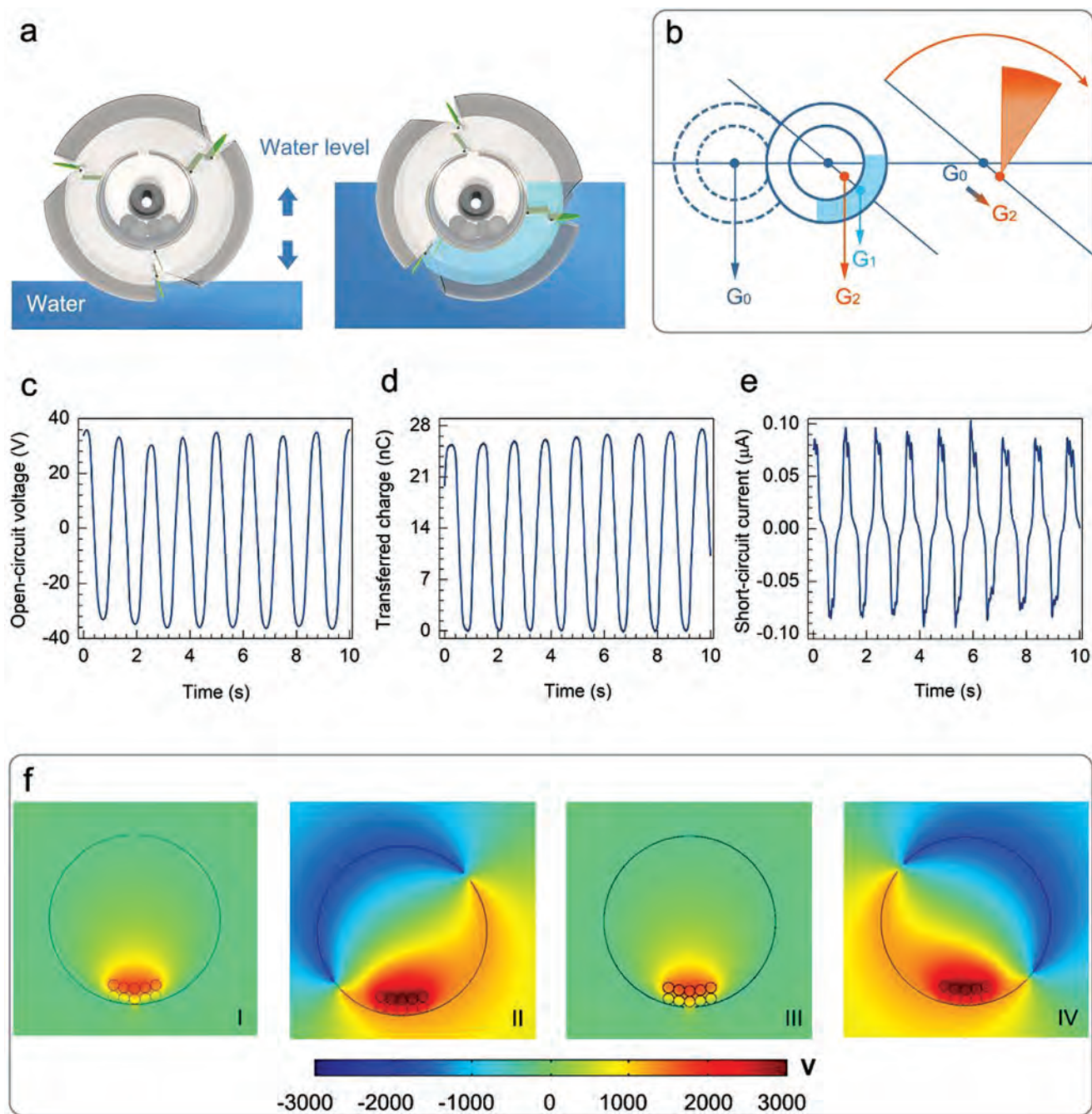


Figure 2. Working principle and typical performance of the BSA-TENG. a) Schematic diagram showing the water inflow status of the BSA-TENG when ocean waves fluctuate up and down. b) Schematic diagram of the BSA-TENG in the barycenter self-adapting process. c) Open-circuit voltage waveform, d) transferred charge waveform, and e) short-circuit current waveform under a continuous mechanical trigger. f) The corresponding potential distribution calculated by COMSOL in a 2D plane.

influences of the inside diameter were systematically studied, and the diagram is specifically expressed in **Figure 3a**. The electrical output performance at different inside diameters from 85 to 150 mm is depicted in **Figure 3b** when using the fluorinated ethylene (FEP) film and three balls with a diameter of 30 mm. As the inside diameter increases, the area of the dielectric film increases, and the electrical output performance increases, reaching a maximum short circuit

current of 0.21 μA , open-circuit voltage of 70 V and transferred charge of 32 nC when the inside diameter is 150 mm. The influence of the ball materials was also investigated, as expressed in **Figure 3c** and **Figure S3b–d** (Supporting Information). The electrical output performances of the BSA-TENG under the aluminum, rubber, and nylon ball materials are depicted in **Figure 3d**, when the dielectric film is FEP and the inside diameter is 150 mm. When the nylon balls are used,

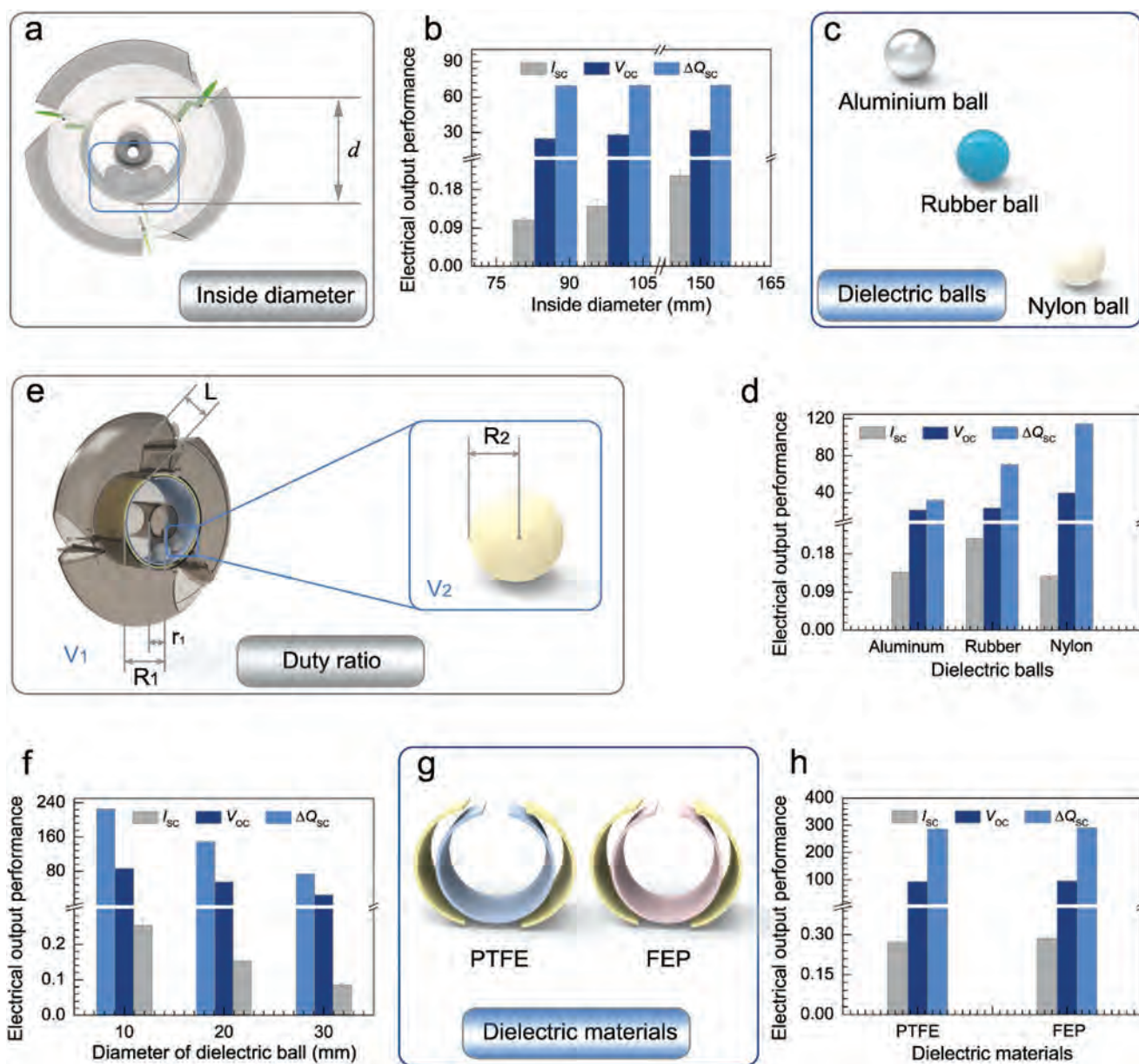


Figure 3. Output performance of the BSA-TENG under different conditions driven by the motor. a) Schematic diagram of the inside diameter of the BSA-TENG. b) The electrical output performance of the BSA-TENG measured at different inside diameters. c) Schematic diagram showing dielectric balls of different materials. d) The electrical output performance of the BSA-TENG measured with different ball materials. e) Illustration diagram of the duty ratio (D). f) The electrical output performance by different diameters of dielectric ball for a duty ratio (D) of 9%. g) Schematic diagram of the BSA-TENG internal structure with different dielectric films. h) The electrical output performance of the BSA-TENG measured at different dielectric films.

the open-circuit voltage and transferred charge reach maxima of 115 V and 40 nC, respectively. However, the short-circuit current is opposite, and the short-circuit current of nylon balls is the lowest, $\approx 0.13 \mu\text{A}$. The mass of each material ball is shown in Table S1 (Supporting Information), and their distinction cannot be ignored; it affects the centrifugal force. The centrifugal force (F) can be written as $F = m \times a$, where m is the mass of the ball and a is the acceleration of the device. A greater mass of aluminum and rubber ball increases their centrifugal force, leading to a better friction and resulting in the current increase.

In addition, the effects of the different dielectric ball quantities on the electrical output performance were also studied under different dielectric ball sizes. Figure S3d–f (Supporting Information) shows photographs of nylon balls of different sizes. As shown in Figure S4 (Supporting Information), at different diameters of nylon balls, the short-circuit current, open-circuit voltage, and transferred charge all increase with increasing ball quantity. However, the larger the diameter of the dielectric balls, the less dielectric balls can be contained in the ring-shaped inner cavity. To consider both the size and

quantity of balls, we introduce a new concept called the duty cycle (denoted as D). $D = nV_2/V_1$, where n is the quantity of dielectric balls, V_1 is the volume of the ring-shaped inner cavity, and V_2 is the volume of dielectric balls, as shown in Figure 3e. Herein, we choose three different conditions with the same duty cycle of 9%. The trends of the short-circuit current, open-circuit voltage, and transferred charge at different quantities of balls under a duty cycle of 9% are depicted in Figure 3f. When the duty cycle is 9%, the greater diameter of balls will decrease the quantity of balls. From 80 balls to 3 balls, the output performances decrease widely; when the quantity of balls is 80, it reaches the maximum short-circuit current of 0.25 μA , open-circuit voltage of 225 V, and transferred charge of 87 nC. This proves that choosing smaller and more balls is beneficial to the output performance of the BSA-TENG. This is also related to the contact area between the balls and dielectric film. When the quantity of balls reaches a certain value, the output performance no longer increases. The quantity of charge generated on the dielectric films will reach the saturation state or the dielectric ball cannot contact the dielectric films completely. The influences of the dielectric film were also investigated, and the materials of the dielectric film are expressed in Figure 3g. Figure 3h shows the open-circuit voltage, short-circuit current, and transferred charge of the BSA-TENG with different dielectric films. When the dielectric film is FEP, the output performance is better, reaching a short circuit current of 0.29 μA , open-circuit voltage of 290 V, and transferred charge of 96 nC. Finally, we chose an inside diameter of 150 mm, FEP as a dielectric film, and 80 nylon balls with a diameter of 10 mm to continue the experiment.

The influences of the rotation speed were also investigated under external mechanical triggers, as shown in Figure 4a. The trends of the output performance at different rotation speeds from 1 to 50 rpm are displayed in Figure 4b–d. The results show that the rotation speed has little effect on the open-circuit voltage and transferred charge. However, the short-circuit current is greatly affected by the rotation speed. When the rotation speed increased from 1 to 50 rpm, the short-circuit current increased ≈ 14 times. Furthermore, various load resistances were connected to the device, and the short-circuit current and open-circuit voltage were measured. According to Figure 4e, the matched resistance and maximum output power of the BSA-TENG are measured at a frequency of ≈ 0.8 Hz. When the external resistance equals the internal impedance, the maximum power reaches 0.1 mW with a load resistance of 500 M Ω . In addition, Figure 4f plots the charging performance of the BSA-TENG with different capacitors. As the capacitance increases, the charging voltage decreases with a reduced charging speed. The voltage of the capacitor of 10 μF can be raised to 3.5 V within 250 s. As depicted in Figure 4g,h and Figure S5 (Supporting Information), the BSA-TENG can drive 600 commercial blue LEDs by pulse-type alternating current, and its process is displayed in Video S2 (Supporting Information).

Figure 5a shows a schematic diagram of the BSA-TENG array. Multiple arrays were ranked to harvest omnidirectional ocean wave energy. To demonstrate the output performance of the BSA-TENG for harvesting ocean wave energy, a

BSA-TENG system device was placed in a water tank to harvest the energy of the simulated water wave (Figure S6a, Supporting Information). When the water wave frequency was below 1 Hz, the output performance of the BSA-TENG in water was 43 V, 22 nC, and 0.02 μA (Figure 5b–d). The BSA-TENG is used to power a digital thermometer and transmitter through circuit connections. A detailed circuit diagram of the BSA-TENG prewarning system is displayed in Figure S6b (Supporting Information). Figure 5e illustrates the charging performance of the BSA-TENG with a 470 μF capacitor. A photo of the BSA-TENG working in the river is shown in Figure S6e (Supporting Information). In addition, Figure 5f and Video S4 (Supporting Information) illustrate that the digital thermometer was successfully powered by the BSA-TENG. Figure 5g and Video S5 (Supporting Information) also illustrate that the BSA-TENG can successfully power the transmitter. Moreover, the durability test is shown in Figure S7 (Supporting Information). Operating over 6000 s under a water wave frequency of ≈ 1 Hz, the voltage hardly changes. These applications indicate the capability of the BSA-TENG in harvesting HEEs from the ocean. This experiment demonstrates the potential of the BSA-TENG for wide use in temperature sensing and seawater wave warning.

3. Conclusions

In summary, we developed a BSA-TENG for high-efficiency harvesting of low-frequency ocean HEEs by a simple physical gravity-guided structure design. Benefitting from the barycenter self-adapting structure, which can effectively convert random vibrational water wave HEE into rotational mechanical energy and then convert into electric energy. More importantly, a significant output performance of the BSA-TENG can be obtained in a nonlinear sea water wave pool that delivers a peak power of 0.1 mW under an external load resistance of 500 M Ω when the working frequency is < 1 Hz. To provide effective analytics and decision for forecasters in marine meteorology, a self-powered temperature sensor and wireless signal transmitter system was realized and driven entirely by the BSA-TENG, which can perform temperature sensing and sea water wave warning. This work demonstrates applications of the BSA-TENG, which are expected to bring a great opportunity in ocean HEE harvesting, opens new avenues for self-powered forecasting services in marine meteorology and sea data statistics, and may profoundly influence global climate observations.

4. Experimental Section

Fabrication of BSA-TENG Device: First, the barycenter self-adapting triboelectric nanogenerator had a diameter of 250 mm and a thickness of 56 mm. The housing baffles and cover were manufactured by 3D Printer (from ZRapid Tech) using white resin material (ABS, hardness of Shore D 82; density of 1.15 g cm $^{-3}$; dielectric strength of 14.7 kV mm $^{-1}$). Then, each housing baffle was fixed to each opening of the housing with two bearings and a shaft. The size of the bearing was an inside diameter of 1 mm and an outside diameter of 3 mm, and the shaft was a length of 56 mm and a diameter of

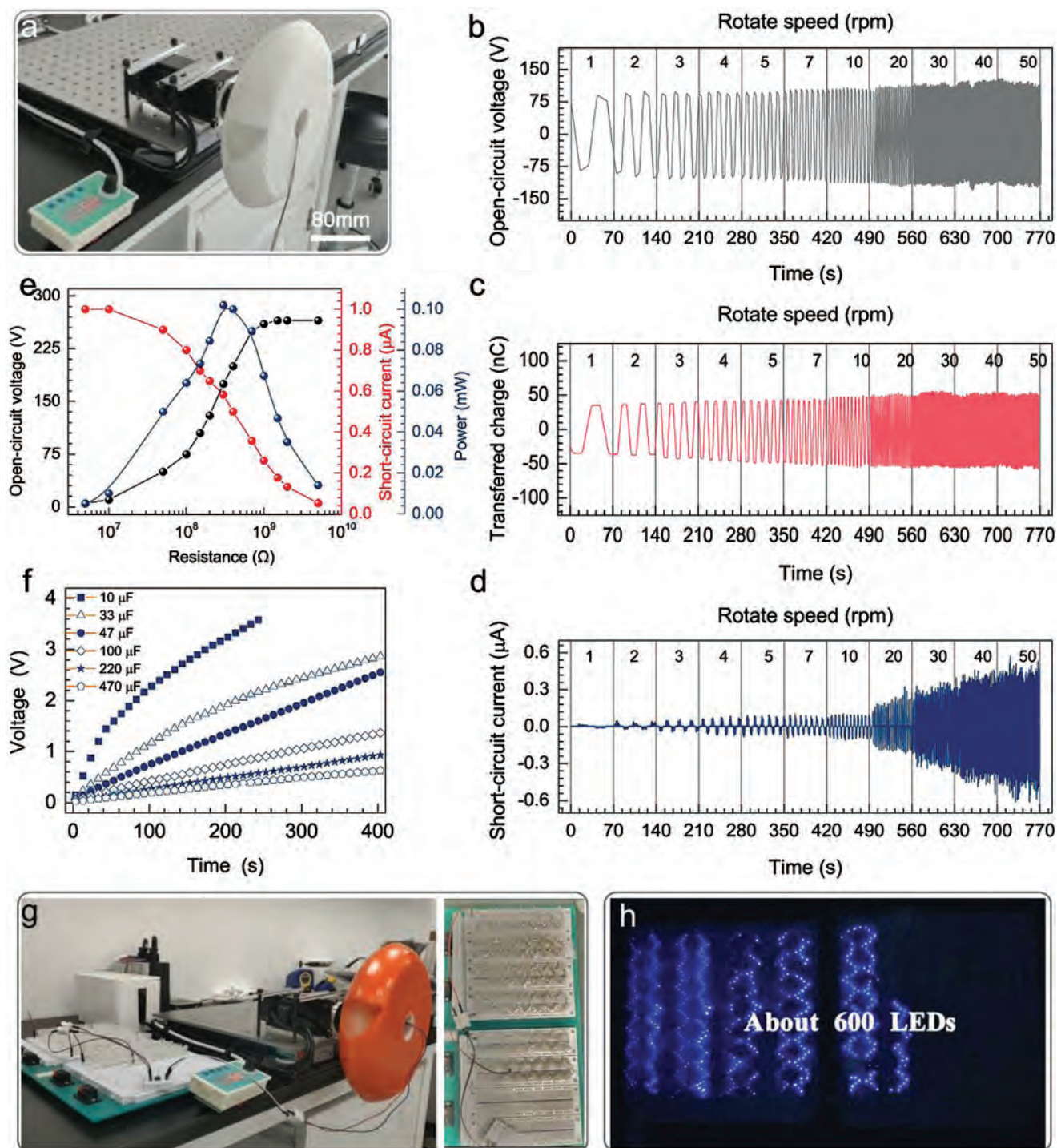


Figure 4. Output performance of the BSA-TENG by mechanical triggering. a) Photo of the mechanical testing process. b) The open-circuit voltage, c) transferred charge and d) short-circuit current of the BSA-TENG measured at different rotation speeds. e) The voltage, current and power output of the BSA-TENG under various external loads. f) Charging voltage of capacitors with various capacitances by the BSA-TENG. g) Working process of the BSA-TENG to power 600 LEDs. h) Photo of the light 600 blue LEDs.

1 mm. Two aluminum electrodes with a thickness of 60 mm and size of 48 mm × 225 mm were symmetrically attached onto the inner arc surface. Furthermore, an FEP film 80 mm in thickness and 48 mm × 470 mm in size was introduced to cover the electrodes. Eighty nylon balls with a diameter of 10 mm were placed inside the

ring-shaped inner cavity. Finally, the cover was glued and sealed with butyl waterproof adhesive to make it completely waterproof.

Characterization and Measurements: The as-fabricated BSA-TENG was mounted on the programmed servo motor (Times Brilliant XK80AEA04030-SCK Servo Motor), which was used as a mechanical

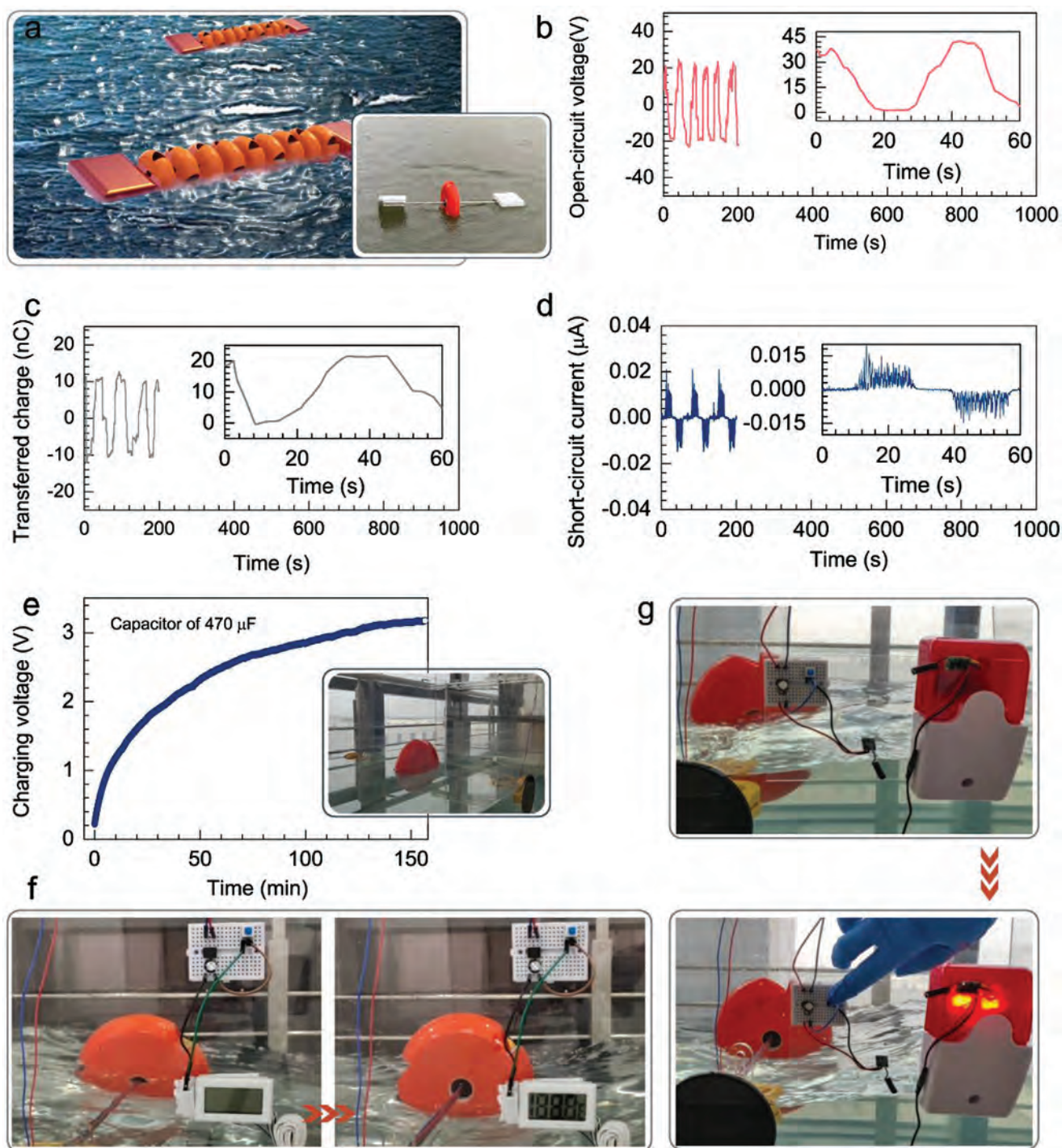


Figure 5. Application and output performance of the BSA-TENG in ocean waves. a) Warning diagram of the BSA-TENG on the ocean surface. b) The open-circuit voltage, c) short-circuit transferred charge, and d) short-circuit current of the BSA-TENG measured in ocean waves. e) The charging performance of the BSA-TENG in ocean waves. f) Powering a digital thermometer by charging a 470 μF capacitor. g) Powering a wireless transmitter by charging a 470 μF capacitor.

trigger condition. The open-circuit voltages, short-circuit currents and transferred charges of the BSA-TENG were measured by low-noise voltage preamplifiers (Keithley 6514 System Electrometer). A programed LabVIEW interface was used to realize real-time data acquisition. The electric outputs of the BSA-TENG device were measured in regular ocean waves. The swing of the push plate was

realized through the rotation of the crank, which was controlled by a servo motor. The rebound wave absorber comprises a slope covered with a porous cushion. The short-circuit current, open-circuit voltage, transferred charge of the device, and charging voltage on a capacitor were all measured by a current preamplifier (Keithley 6514 System Electrometer).

Supporting Information

Supporting Information is available from the Wiley Online Library or from the author.

Acknowledgements

The research was sponsored by the Natural Science Foundation of Beijing Municipality (2192062), the National Key R & D Project from Minister of Science and Technology (2021YFA1201601), and National Natural Science Foundation of China (52192610).

Conflict of Interest

The authors declare no conflict of interest.

Author Contributions

Y.Y. and J.W. contributed equally to this work. Y.Y. prepared the original draft and methodology. J.W. was associated with data curation and validation. F.C. was associated with investigation and formal analysis. X.G. was associated with visualization. Y.H. was associated with validation. T.J. was associated with methodology and formal analysis. B.C. reviewed and edited the final manuscript, and was associated with supervision and resources. Z.L.W. was associated with conceptualization, supervision, resources, and reviewed and edited the final manuscript.

Data Availability Statement

The data that support the findings of this study are available from the corresponding author upon reasonable request.

Keywords

high entropy energy, self-adapting, self-powered forecasting systems, triboelectric nanogenerators

Received: January 13, 2022

Revised: February 17, 2022

Published online:

- [1] L. Atzori, A. Iera, G. Morabito, *Comput. Networks* **2010**, *54*, 2787.
- [2] Z. L. Wang, *Nano Energy* **2019**, *58*, 669.
- [3] Y. Feng, J. Han, M. Xu, X. Liang, T. Jiang, H. Li, Z. L. Wang, *Adv. Energy Mater.* **2021**.
- [4] Y. Li, X. Chen, J. Yu, *Processes* **2019**, *7*, 69.
- [5] L. Liu, X. Guo, C. Lee, *Nano Energy* **2021**, *88*, 106304.
- [6] T. X. Xiao, X. Liang, T. Jiang, L. Xu, J. J. Shao, J. H. Nie, Y. Bai, W. Zhong, Z. L. Wang, *Adv. Funct. Mater.* **2018**, *28*, 1802634.
- [7] G. Liu, L. Xiao, C. Chen, W. Liu, X. Pu, Z. Wu, C. Hu, Z. L. Wang, *Nano Energy* **2020**, *75*, 104975.
- [8] Y. Wang, X. Liu, Y. Wang, H. Wang, H. Wang, S. L. Zhang, T. Zhao, M. Xu, Z. L. Wang, *ACS Nano* **2021**, *15*, 15700.
- [9] Y. Wang, X. Liu, T. Chen, H. Wang, C. Zhu, H. Yu, L. Song, X. Pan, J. Mi, C. Lee, M. Xu, *Nano Energy* **2021**, *90*, 106503.
- [10] S. L. Zhang, M. Xu, C. Zhang, Y. Wang, H. Zou, X. He, Z. Wang, Z. L. Wang, *Nano Energy* **2018**, *48*, 421.
- [11] X. Liang, T. Jiang, Y. Feng, P. Lu, J. An, Z. L. Wang, *Adv. Energy Mater.* **2020**, *10*, 2002123.
- [12] J. Tian, X. Chen, Z. L. Wang, *Nanotechnology* **2020**, *31*, 242001.
- [13] J. Chen, H. Guo, C. Hu, Z. L. Wang, *Adv. Energy Mater.* **2020**, *10*, 2000886.
- [14] L. Liu, Q. Shi, J. S. Ho, C. Lee, *Nano Energy* **2019**, *66*, 104167.
- [15] C. Hou, T. Chen, Y. Li, M. Huang, Q. Shi, H. Liu, L. Sun, C. Lee, *Nano Energy* **2019**, *63*, 103871.
- [16] C. Zhang, L. He, L. Zhou, O. Yang, W. Yuan, X. Wei, Y. Liu, L. Lu, J. Wang, Z. L. Wang, *Joule* **2021**, *5*, 1613.
- [17] B. D. Chen, W. Tang, C. He, C. R. Deng, L. J. Yang, L. P. Zhu, J. Chen, J. J. Shao, L. Liu, Z. L. Wang, *Mater. Today* **2018**, *21*, 88.
- [18] a) K. Han, J. Luo, J. Chen, B. Chen, L. Xu, Y. Feng, W. Tang, Z. L. Wang, *Microsyst. Nanoeng.* **2021**, *7*, 7; b) C. Zhang, L. Liu, L. Zhou, X. Yin, X. Wei, Y. Hu, Y. Liu, S. Chen, J. Wang, Z. L. Wang, *ACS Nano* **2020**, *14*, 7092.
- [19] X. Liang, Z. Liu, Y. Feng, J. Han, L. Li, J. An, P. Chen, T. Jiang, Z. L. Wang, *Nano Energy* **2021**, *83*, 105836.
- [20] L. Liu, Q. Shi, C. Lee, *Nano Energy* **2020**, *76*, 105052.
- [21] a) J. An, Z. M. Wang, T. Jiang, X. Liang, Z. L. Wang, *Adv. Funct. Mater.* **2019**, *29*, 1904867; b) P. Cheng, H. Guo, Z. Wen, C. Zhang, X. Yin, X. Li, D. Liu, W. Song, X. Sun, J. Wang, Z. L. Wang, *Nano Energy* **2019**, *57*, 432; c) S. Leung, H. Fu, M. Zhang, A. H. Hassan, T. Jiang, K. N. Salama, Z. L. Wang, J. He, *Energy Environ. Sci.* **2020**, *13*, 1300; d) X. Liang, T. Jiang, G. Liu, Y. Feng, C. Zhang, Z. L. Wang, *Energy Environ. Sci.* **2020**, *13*, 277; e) X. Liang, T. Jiang, G. Liu, T. Xiao, L. Xu, W. Li, F. Xi, C. Zhang, Z. L. Wang, *Adv. Funct. Mater.* **2019**, *29*, 1807241; f) X. Yang, L. Xu, P. Lin, W. Zhong, Y. Bai, J. Luo, J. Chen, Z. L. Wang, *Nano Energy* **2019**, *60*, 404; g) L. Xu, T. Jiang, P. Lin, J. J. Shao, C. He, W. Zhong, X. Y. Chen, Z. L. Wang, *ACS Nano* **2018**, *12*, 1849.
- [22] Z. L. Wang, T. Jiang, L. Xu, *Nano Energy* **2017**, *39*, 9.